

X-shooter spectroscopy of Liller 1 giant stars [★]

D. A. **Alvarez**^{1,2}, C. **Fabrizio**², L. **Ogden**², C. **Phillips**^{1,2}, A. **Mach**^{1,2}, L. **Cifuentes**^{1,2}, C. **Chiappini**^{1,2}, B. **Lind**^{1,2}, F. R. **Fornari**^{1,2}, R. M. **Ribera**³, E. **Delfino**

¹ Dipartimento di Fisica e Astronomia, Università di Bologna, I-40129 Bologna, Italy
e-mail: deimer.alvarezgaray2@unibo.it
² INAF, Osservatorio Astronomico di Bologna, I-40129 Bologna, Italy
³ Department of Physics and Astronomy, University of California, Los Angeles, CA 90095-1547, USA

ApJ, 2024

ABSTRACT

We present X-shooter spectroscopy of 27 Liller 1 (L1) stars in the Galactic Bulge. The stars are located at a distance of 2.2 ± 0.2 kpc from the Sun. We measure the metallicity $\langle [Fe/H] \rangle = -0.31 \pm 0.02$ dex and the alpha-element abundance $\langle [\alpha/Fe] \rangle = +0.22 \pm 0.03$ dex. We also measure the abundances of Na, V, Cr, Mn, Ni, and Co. The stars show a clear trend of increasing alpha-element abundance with increasing metallicity. We also measure the carbon-to-oxygen ratio $[C/O]$ and the $^{12}C/^{13}C$ ratio. The stars are located in the red giant branch (RGB) and the red clump (RC) of the Liller 1 cluster. The stars are located in the Galactic Bulge, which is a region of high stellar density and metallicity. The stars are located in the Galactic Bulge, which is a region of high stellar density and metallicity.

Key words. Stars: Population II; Stars: Clusters: Open; Stars: Clusters: Globular

1. Introduction

Liller 1 is a Galactic Bulge cluster located at a distance of 2.2 ± 0.2 kpc from the Sun. The cluster is located in the Galactic Bulge, which is a region of high stellar density and metallicity. The cluster is located in the Galactic Bulge, which is a region of high stellar density and metallicity.

A color-magnitude diagram (CMD) from the Gaia DR3 data shows the cluster's structure. The cluster is located in the Galactic Bulge, which is a region of high stellar density and metallicity. The cluster is located in the Galactic Bulge, which is a region of high stellar density and metallicity.

[★] Based on data collected with the X-shooter instrument on board the Very Large Telescope (VLT) at the European Southern Observatory (ESO), Chile. Project ID: 089.D-0306 (PI: F. R. Fornari).

The cluster is located in the Galactic Bulge, which is a region of high stellar density and metallicity. The cluster is located in the Galactic Bulge, which is a region of high stellar density and metallicity. The cluster is located in the Galactic Bulge, which is a region of high stellar density and metallicity.

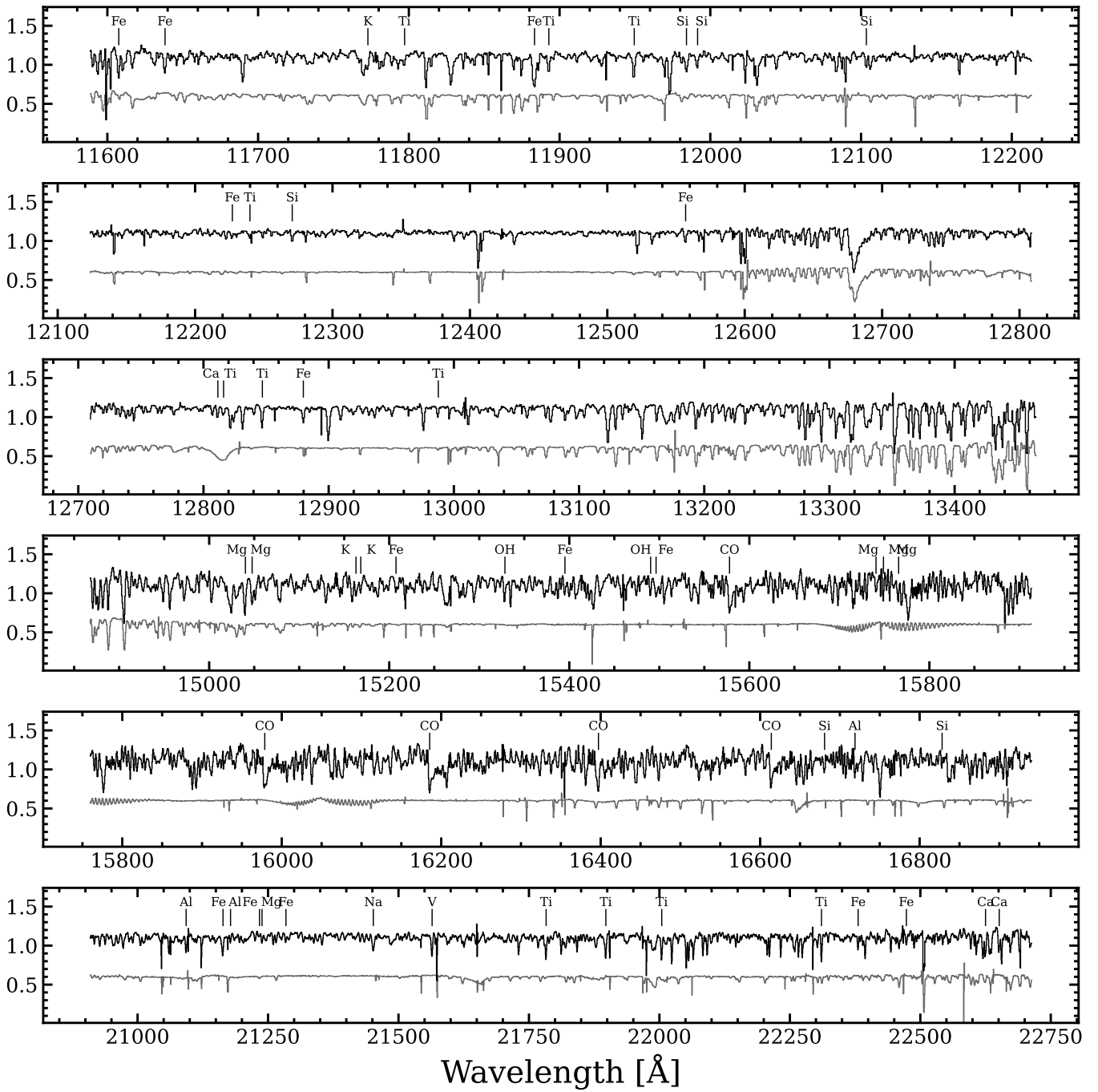


Fig. 1. Photometry of a 3400 K star, H, and K lines.

Introduction

... (2018); ... (2019); ... (2022); ... (2023), ...

2. Observations

... (PI: F.R.) ... $\approx 8,000$... μm ...

Table 1. Observed

ID	RA D _g	Dec D _g	J In	K In	μ In
20	263.3413160	-33.3917580	12.27	9.15	34.3
24	263.3580030	-33.3844380	12.03	9.26	25.0
27	263.3463770	-33.3867450	11.97	9.22	20.6
31	263.3386050	-33.3953320	12.10	9.29	46.4
34	263.3370940	-33.3755720	12.07	9.30	68.0
35	263.3561440	-33.3858760	12.12	9.28	17.6
37	263.3408550	-33.3894200	12.21	9.36	34.6
39	263.3619960	-33.3893320	12.20	9.26	28.9
45	263.3540437	-33.3894655	12.02	9.48	5.3
48	263.3509838	-33.3909300	12.41	8.98	6.6
62	263.3659950	-33.4061700	12.50	9.75	72.6
66	263.3614350	-33.4098700	12.50	9.78	78.3
68	263.3392510	-33.4054300	12.46	9.78	69.5
71	263.3535490	-33.3906021	12.43	9.87	5.2
74	263.3490706	-33.3910950	12.80	10.01	11.4
79	263.3491370	-33.3856470	12.65	10.02	17.4
85	263.3551136	-33.3912034	12.84	9.95	10.3
88	263.3537148	-33.3957827	12.80	10.01	22.9
98	263.3560121	-33.3878820	12.98	10.41	12.6
100	263.3440470	-33.3914300	13.00	10.38	26.2
103	263.3554470	-33.3868030	13.07	10.33	13.4
104	263.3478150	-33.3866650	13.13	10.49	17.3
108	263.3515430	-33.4021070	13.06	10.31	45.5
109	263.3548662	-33.3878013	13.08	10.60	9.8
115	263.3599230	-33.3909680	13.14	10.36	22.9
120	263.3599690	-33.3839110	13.16	10.44	30.2
121	263.3404830	-33.3814510	13.09	10.47	46.1
124	263.3421180	-33.4040030	13.11	10.49	60.6
126	263.3496644	-33.3857118	13.32	10.71	16.0
132	263.3630190	-33.4004900	13.25	10.65	50.8
136	263.3545365	-33.3861169	13.46	10.78	13.8
145	263.3499870	-33.3816380	13.45	10.83	29.3
148	263.3529737	-33.3828074	13.48	11.15	24.1
149	263.3629250	-33.4037590	13.50	10.85	60.5

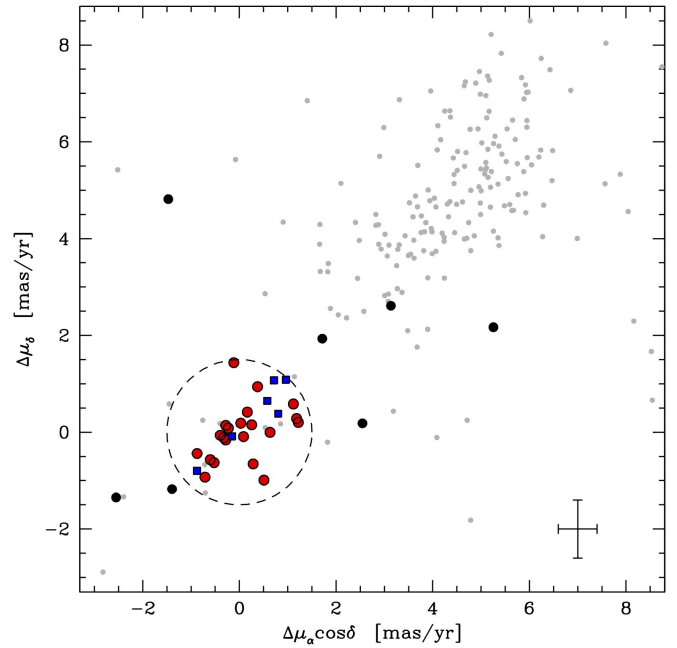


Fig. 2. Proper motion components $\Delta\mu_\alpha \cos \delta$ [mas/yr] vs $\Delta\mu_\delta$ [mas/yr] for the sample of 149 stars. The dashed circle indicates the region $\Delta\mu_\alpha \cos \delta < 1.9$ mas/yr and $|\Delta\mu_\delta| < 1.9$ mas/yr. The red and blue points represent the stars with $\mu_\alpha \cos \delta < 0$ and $\mu_\alpha \cos \delta > 0$, respectively. The crosshair symbol indicates the position of the star HD 10180.

The proper motion components $\mu_\alpha \cos \delta$ and μ_δ were derived from the Gaia DR3 astrometric solution (Gaia Collaboration et al. 2018). The proper motion errors were estimated using the method described in Gaia Collaboration et al. (2016). The proper motion errors were estimated using the method described in Gaia Collaboration et al. (2016). The proper motion errors were estimated using the method described in Gaia Collaboration et al. (2016).

3. Stellar membership from proper motions

The proper motion components $\mu_\alpha \cos \delta$ and μ_δ were derived from the Gaia DR3 astrometric solution (Gaia Collaboration et al. 2018). The proper motion errors were estimated using the method described in Gaia Collaboration et al. (2016). The proper motion errors were estimated using the method described in Gaia Collaboration et al. (2016).

The proper motion components $\mu_\alpha \cos \delta$ and μ_δ were derived from the Gaia DR3 astrometric solution (Gaia Collaboration et al. 2018). The proper motion errors were estimated using the method described in Gaia Collaboration et al. (2016). The proper motion errors were estimated using the method described in Gaia Collaboration et al. (2016). The proper motion errors were estimated using the method described in Gaia Collaboration et al. (2016).

4. Spectral analysis

The NIR color indices $J-K$ and $H-K$ were derived from the Gaia DR3 photometry (Gaia Collaboration et al. 2018). The color indices were derived from the Gaia DR3 photometry (Gaia Collaboration et al. 2018).

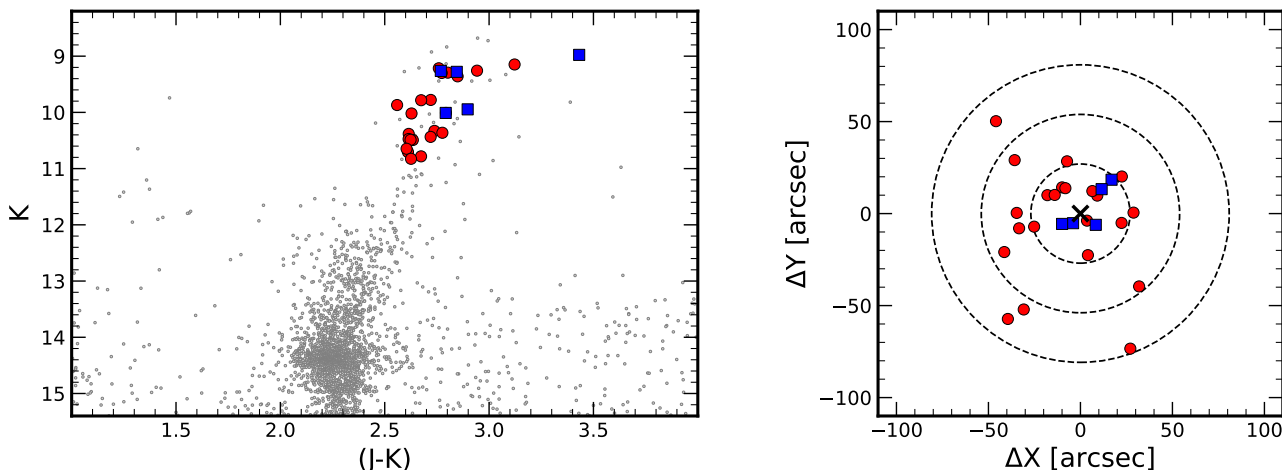


Fig. 3. Photometric selection of the cluster stars in the K vs $(J-K)$ CMD (left plot) and in the ΔY vs ΔX plot (right plot). The cluster is located at $\alpha = 263^{\circ}3523333$, $\delta = -33^{\circ}3895556$, $d = 10$ pc, $r_c = 5''.39$ (Bica et al. 2015).

The cluster stars were selected using the RBOECRM (A&P 1998; Plez 2012), MARCS (Girard 2008), and the K vs $(J-K)$ CMD (Bica et al. 2015). The cluster is located at $\alpha = 263^{\circ}3523333$, $\delta = -33^{\circ}3895556$, $d = 10$ pc, $r_c = 5''.39$ (Bica et al. 2015). The cluster stars were selected using the RBOECRM (A&P 1998; Plez 2012), MARCS (Girard 2008), and the K vs $(J-K)$ CMD (Bica et al. 2015). The cluster is located at $\alpha = 263^{\circ}3523333$, $\delta = -33^{\circ}3895556$, $d = 10$ pc, $r_c = 5''.39$ (Bica et al. 2015).

4.1. Stellar parameters

The cluster stars were selected using the RBOECRM (A&P 1998; Plez 2012), MARCS (Girard 2008), and the K vs $(J-K)$ CMD (Bica et al. 2015). The cluster is located at $\alpha = 263^{\circ}3523333$, $\delta = -33^{\circ}3895556$, $d = 10$ pc, $r_c = 5''.39$ (Bica et al. 2015). The cluster stars were selected using the RBOECRM (A&P 1998; Plez 2012), MARCS (Girard 2008), and the K vs $(J-K)$ CMD (Bica et al. 2015). The cluster is located at $\alpha = 263^{\circ}3523333$, $\delta = -33^{\circ}3895556$, $d = 10$ pc, $r_c = 5''.39$ (Bica et al. 2015).

The cluster stars were selected using the RBOECRM (A&P 1998; Plez 2012), MARCS (Girard 2008), and the K vs $(J-K)$ CMD (Bica et al. 2015). The cluster is located at $\alpha = 263^{\circ}3523333$, $\delta = -33^{\circ}3895556$, $d = 10$ pc, $r_c = 5''.39$ (Bica et al. 2015). The cluster stars were selected using the RBOECRM (A&P 1998; Plez 2012), MARCS (Girard 2008), and the K vs $(J-K)$ CMD (Bica et al. 2015). The cluster is located at $\alpha = 263^{\circ}3523333$, $\delta = -33^{\circ}3895556$, $d = 10$ pc, $r_c = 5''.39$ (Bica et al. 2015).

4.2. Continuum normalization

The cluster stars were selected using the RBOECRM (A&P 1998; Plez 2012), MARCS (Girard 2008), and the K vs $(J-K)$ CMD (Bica et al. 2015). The cluster is located at $\alpha = 263^{\circ}3523333$, $\delta = -33^{\circ}3895556$, $d = 10$ pc, $r_c = 5''.39$ (Bica et al. 2015). The cluster stars were selected using the RBOECRM (A&P 1998; Plez 2012), MARCS (Girard 2008), and the K vs $(J-K)$ CMD (Bica et al. 2015). The cluster is located at $\alpha = 263^{\circ}3523333$, $\delta = -33^{\circ}3895556$, $d = 10$ pc, $r_c = 5''.39$ (Bica et al. 2015).

¹ <https://www.lupm.in2p3.fr/users/plez/>

Table 2. Parameters.

ID	T_{eff}	RV	Fe /H]	C /H]	O /H]	Na /H]	Mg /H]	Al /H]	S /H]	K /H]	Ca /H]	Ti /H]	V /H]	$^{12}\text{C}/^{13}\text{C}$
	[K]	km s^{-1}	7.50	8.56	8.77	6.29	7.55	6.43	7.59	5.14	6.37	4.94	3.89	89
20	3400	52	-0.28±0.08	-0.42±0.10	+0.19±0.06	+0.32±0.07	+0.12±0.10	+0.08±0.10	+0.02±0.08	+0.14±0.10	+0.21±0.10	+0.26±0.12	-0.05±0.10	5.3±1.4
24	3400	86	+0.24±0.07	-0.10±0.03	+0.28±0.02	+0.80±0.10	+0.27±0.06	+0.41±0.10	+0.20±0.04	+0.21±0.06	+0.25±0.06	+0.33±0.04	+0.34±0.10	7.4±1.7
27	3400	69	-0.38±0.06	-0.78±0.04	-0.01±0.10	+0.03±0.03	+0.16±0.05	+0.01±0.05	-0.17±0.04	+0.02±0.05	+0.08±0.10	+0.23±0.08	-0.33±0.10	9.2±1.2
31	3400	60	-0.24±0.06	-0.74±0.10	+0.09±0.06	+0.17±0.04	+0.06±0.09	+0.03±0.06	+0.07±0.10	+0.11±0.12	+0.03±0.10	+0.31±0.05	-0.21±0.10	9.4±2.0
34	3400	76	-0.28±0.07	-1.04±0.07	+0.11±0.06	+0.29±0.11	+0.23±0.06	-0.01±0.10	-0.03±0.01	+0.25±0.10	+0.23±0.10	+0.13±0.07	-0.19±0.10	7.9±1.3
35	3400	86	+0.20±0.06	-0.17±0.03	+0.19±0.06	+0.74±0.10	+0.15±0.10	+0.34±0.10	+0.17±0.06	+0.07±0.10	+0.16±0.10	+0.47±0.05	+0.30±0.10	12.3±1.8
37	3400	61	-0.33±0.07	-0.58±0.06	+0.11±0.10	-0.09±0.04	+0.18±0.05	+0.07±0.10	-0.14±0.05	-0.06±0.03	+0.13±0.10	+0.13±0.09	-0.37±0.10	6.8±1.6
39	3400	55	-0.29±0.09	-0.75±0.07	+0.12±0.10	+0.28±0.10	+0.19±0.09	+0.02±0.05	-0.03±0.06	-	+0.02±0.10	+0.30±0.07	-0.19±0.10	10.5±1.3
48	3400	42	+0.13±0.08	-0.22±0.06	+0.14±0.10	+0.74±0.10	+0.25±0.10	+0.25±0.06	+0.15±0.05	+0.15±0.10	+0.15±0.10	+0.22±0.07	+0.06±0.10	11.3±1.2
66	3500	99	-0.06±0.05	-0.20±0.05	+0.09±0.06	+0.57±0.10	+0.19±0.04	+0.18±0.10	+0.14±0.06	+0.21±0.10	-	-	+0.17±0.10	10.9±1.5
68	3500	78	-0.36±0.05	-0.63±0.05	-0.06±0.08	-0.04±0.10	+0.06±0.06	+0.05±0.10	-0.19±0.05	-0.12±0.10	+0.03±0.10	+0.18±0.09	-0.43±0.10	7.0±1.6
71	3500	53	-0.40±0.08	-0.87±0.04	-0.17±0.07	-0.18±0.10	-0.13±0.05	-0.13±0.06	-0.07±0.04	-0.12±0.10	-0.05±0.10	-0.05±0.05	-0.53±0.10	7.6±1.0
74	3500	70	+0.30±0.06	-0.13±0.03	+0.25±0.07	+0.95±0.10	+0.32±0.10	+0.38±0.10	+0.21±0.05	+0.11±0.10	+0.31±0.10	+0.39±0.05	+0.22±0.10	10.5±1.8
79	3600	70	-0.22±0.05	-0.97±0.10	-0.05±0.10	+0.01±0.10	+0.11±0.10	+0.12±0.10	+0.06±0.08	+0.30±0.10	-	+0.19±0.08	-0.47±0.10	8.4±1.0
85	3500	61	+0.22±0.07	-0.11±0.10	+0.12±0.06	+0.84±0.10	+0.25±0.05	+0.27±0.10	+0.18±0.04	+0.10±0.10	+0.24±0.10	+0.30±0.10	+0.14±0.10	9.4±1.9
88	3600	72	-0.34±0.08	-0.67±0.04	+0.12±0.10	+0.02±0.10	+0.05±0.10	+0.12±0.08	-0.05±0.04	+0.06±0.10	+0.02±0.07	+0.07±0.04	-0.29±0.10	8.2±1.7
100	3700	68	-0.42±0.08	-1.17±0.07	-0.27±0.08	+0.13±0.10	-0.03±0.10	+0.00±0.08	-0.13±0.05	-0.08±0.06	-0.23±0.10	-0.02±0.08	-0.35±0.10	9.2±1.7
103	3700	40	-0.38±0.07	-0.62±0.04	+0.03±0.06	-0.04±0.10	-0.01±0.10	+0.16±0.05	-0.12±0.05	+0.13±0.10	-0.05±0.10	+0.06±0.04	-0.35±0.10	11.5±2.3
104	3700	57	-0.38±0.06	-0.68±0.05	+0.01±0.07	-0.04±0.10	-0.08±0.10	-0.07±0.05	-0.16±0.10	+0.12±0.10	-0.14±0.10	-0.08±0.10	-0.42±0.10	9.2±1.5
115	3700	57	-0.26±0.09	-0.96±0.10	-0.10±0.10	-	+0.15±0.05	+0.19±0.06	-0.02±0.09	-0.08±0.10	+0.01±0.04	+0.21±0.04	-0.21±0.10	8.2±1.3
120	3700	68	-0.31±0.07	-0.84±0.10	-0.10±0.05	+0.46±0.10	+0.10±0.10	+0.18±0.10	+0.04±0.05	-0.06±0.10	+0.03±0.05	+0.11±0.06	-0.34±0.10	10.5±1.4
121	3700	62	-0.30±0.07	-0.65±0.04	+0.04±0.06	+0.09±0.10	+0.03±0.10	+0.03±0.10	-0.06±0.04	-0.13±0.10	-0.05±0.05	+0.15±0.04	-0.34±0.10	10.9±2.0
124	3700	57	-0.32±0.07	-0.67±0.06	+0.04±0.07	+0.05±0.10	+0.07±0.10	+0.02±0.05	-0.03±0.06	+0.14±0.10	+0.13±0.10	+0.19±0.05	-0.31±0.10	10.5±1.5
126	3700	72	-0.42±0.05	-0.80±0.05	-0.13±0.08	-0.15±0.10	-0.15±0.05	-0.19±0.10	-0.18±0.10	+0.03±0.06	+0.08±0.10	+0.09±0.10	-0.41±0.10	8.4±1.1
132	3700	66	-0.26±0.08	-0.70±0.05	-0.03±0.07	+0.00±0.10	+0.13±0.05	+0.11±0.06	+0.06±0.07	+0.10±0.06	+0.11±0.06	+0.18±0.05	-0.37±0.10	7.6±1.8
136	3800	55	-0.29±0.09	-1.06±0.04	-0.10±0.10	+0.37±0.10	+0.10±0.10	+0.07±0.10	-0.10±0.10	+0.16±0.10	+0.03±0.10	+0.16±0.07	-0.33±0.10	10.0±1.5
145	3800	74	-0.36±0.07	-0.71±0.07	-0.17±0.06	-0.05±0.10	+0.11±0.05	+0.25±0.05	-0.11±0.06	+0.13±0.10	+0.06±0.10	+0.08±0.10	-0.42±0.10	12.1±3.1

Notes. (Mg) (2022) definition.

4.3. Chemical analysis

From the spectra, we derived the abundances of 14 elements: H, K, Na, Mg, Al, Si, S, Ca, Ti, V, Cr, Fe, Ni, and Co. The abundances of these elements are given in Table 2. The abundances of the elements are given in Table 2. The abundances of the elements are given in Table 2.

With the help of the abundance ratios, we can identify the population of the cluster. The abundance ratios of the elements are given in Table 2. The abundance ratios of the elements are given in Table 2.

The abundance ratios of the elements are given in Table 2. The abundance ratios of the elements are given in Table 2. The abundance ratios of the elements are given in Table 2.

The abundance ratios of the elements are given in Table 2. The abundance ratios of the elements are given in Table 2. The abundance ratios of the elements are given in Table 2.

2%; (4.2) (2-3%, (30-50;

5.2. Parameters

The parameters of the cluster are given in Table 2. The parameters of the cluster are given in Table 2. The parameters of the cluster are given in Table 2.

5. Results

The parameters of the cluster are given in Table 2. The parameters of the cluster are given in Table 2. The parameters of the cluster are given in Table 2.

5.1. Radial velocities

The radial velocities of the cluster are given in Table 2. The radial velocities of the cluster are given in Table 2. The radial velocities of the cluster are given in Table 2.

² Fundamental parameters of Galactic globular clusters, <https://people.smp.uq.edu.au/HolgerBaumgardt/globular/>

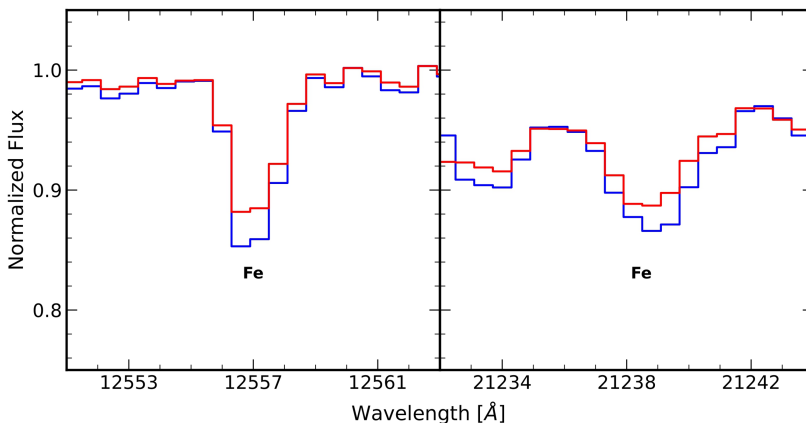
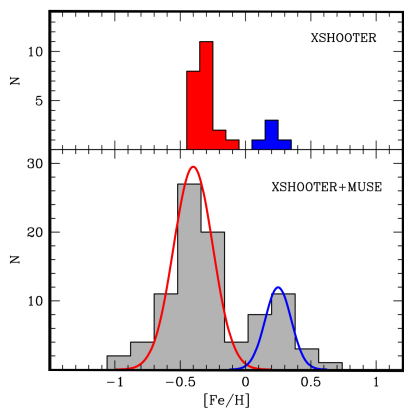


Fig. 4. Histogram of the $[Fe/H]$ distribution for the XSHOOTER (top) and XSHOOTER+MUSE (bottom) samples. The XSHOOTER sample is from the study of [Carr et al. \(2023\)](#), and the XSHOOTER+MUSE sample is from the study of [J et al. \(2019\)](#), and [Carr et al. \(2025\)](#). The XSHOOTER+MUSE sample is from the study of [Carr et al. \(2025\)](#).

5.2. Abundances and abundance ratios

The iron abundance $[Fe/H]$ is determined using the Fe lines in the XSHOOTER spectra. The mean $[Fe/H]$ for the XSHOOTER sample is -0.31 ± 0.02 dex, and for the XSHOOTER+MUSE sample is $+0.22 \pm 0.03$ dex. The scatter in $[Fe/H]$ is $\sigma = 0.06 \pm 0.02$ dex for the XSHOOTER sample and $\sigma = 0.08 \pm 0.01$ dex for the XSHOOTER+MUSE sample. The $[Fe/H]$ distribution is shown in Figure 4.

The carbon abundance $[C/H]$ is determined using the $^{12}C/^{13}C$ ratio in the CO lines. The mean $[C/H]$ for the XSHOOTER sample is 0.11 ± 0.01 dex, and for the XSHOOTER+MUSE sample is 0.05 ± 0.01 dex. The scatter in $[C/H]$ is $\sigma = 0.01$ dex for the XSHOOTER sample and $\sigma = 0.01$ dex for the XSHOOTER+MUSE sample. The $[C/H]$ distribution is shown in Figure 5.

The oxygen abundance $[O/H]$ is determined using the $^{12}O/^{16}O$ ratio in the CO lines. The mean $[O/H]$ for the XSHOOTER sample is 0.42 ± 0.02 dex, and for the XSHOOTER+MUSE sample is 0.60 ± 0.02 dex. The scatter in $[O/H]$ is $\sigma = 0.04$ dex for the XSHOOTER sample and $\sigma = 0.04$ dex for the XSHOOTER+MUSE sample. The $[O/H]$ distribution is shown in Figure 6.

The nitrogen abundance $[N/H]$ is determined using the $^{14}N/^{15}N$ ratio in the CO lines. The mean $[N/H]$ for the XSHOOTER sample is 0.16 ± 0.02 dex, and for the XSHOOTER+MUSE sample is 0.16 ± 0.02 dex. The scatter in $[N/H]$ is $\sigma = 0.02$ dex for the XSHOOTER sample and $\sigma = 0.02$ dex for the XSHOOTER+MUSE sample. The $[N/H]$ distribution is shown in Figure 7.

The alpha element abundance $[alpha/H]$ is determined using the $^{24}Mg/^{28}Si$ ratio in the CO lines. The mean $[alpha/H]$ for the XSHOOTER sample is 0.05 ± 0.01 dex, and for the XSHOOTER+MUSE sample is 0.05 ± 0.01 dex. The scatter in $[alpha/H]$ is $\sigma = 0.01$ dex for the XSHOOTER sample and $\sigma = 0.01$ dex for the XSHOOTER+MUSE sample. The $[alpha/H]$ distribution is shown in Figure 8.

The $^{12}C/^{13}C$ ratio is determined using the $^{12}C/^{13}C$ ratio in the CO lines. The mean $^{12}C/^{13}C$ ratio for the XSHOOTER sample is 10.11 ± 0.01 , and for the XSHOOTER+MUSE sample is 10.05 ± 0.01 . The scatter in $^{12}C/^{13}C$ is $\sigma = 0.01$ for the XSHOOTER sample and $\sigma = 0.01$ for the XSHOOTER+MUSE sample. The $^{12}C/^{13}C$ distribution is shown in Figure 9.

The ^{12}CO and ^{13}CO lines are used to determine the carbon abundance. The mean ^{12}CO and ^{13}CO line ratios for the XSHOOTER sample are 0.11 ± 0.01 and 0.05 ± 0.01 , respectively, and for the XSHOOTER+MUSE sample are 0.11 ± 0.01 and 0.05 ± 0.01 , respectively. The scatter in ^{12}CO and ^{13}CO line ratios is $\sigma = 0.01$ for the XSHOOTER sample and $\sigma = 0.01$ for the XSHOOTER+MUSE sample. The ^{12}CO and ^{13}CO line ratio distribution is shown in Figure 10.

The iron abundance $[Fe/H]$ is determined using the Fe lines in the XSHOOTER spectra. The mean $[Fe/H]$ for the XSHOOTER sample is -0.31 ± 0.02 dex, and for the XSHOOTER+MUSE sample is $+0.22 \pm 0.03$ dex. The scatter in $[Fe/H]$ is $\sigma = 0.06 \pm 0.02$ dex for the XSHOOTER sample and $\sigma = 0.08 \pm 0.01$ dex for the XSHOOTER+MUSE sample. The $[Fe/H]$ distribution is shown in Figure 4.

The carbon abundance $[C/H]$ is determined using the $^{12}C/^{13}C$ ratio in the CO lines. The mean $[C/H]$ for the XSHOOTER sample is 0.11 ± 0.01 dex, and for the XSHOOTER+MUSE sample is 0.05 ± 0.01 dex. The scatter in $[C/H]$ is $\sigma = 0.01$ dex for the XSHOOTER sample and $\sigma = 0.01$ dex for the XSHOOTER+MUSE sample. The $[C/H]$ distribution is shown in Figure 5.

The oxygen abundance $[O/H]$ is determined using the $^{12}O/^{16}O$ ratio in the CO lines. The mean $[O/H]$ for the XSHOOTER sample is 0.42 ± 0.02 dex, and for the XSHOOTER+MUSE sample is 0.60 ± 0.02 dex. The scatter in $[O/H]$ is $\sigma = 0.04$ dex for the XSHOOTER sample and $\sigma = 0.04$ dex for the XSHOOTER+MUSE sample. The $[O/H]$ distribution is shown in Figure 6.

The nitrogen abundance $[N/H]$ is determined using the $^{14}N/^{15}N$ ratio in the CO lines. The mean $[N/H]$ for the XSHOOTER sample is 0.16 ± 0.02 dex, and for the XSHOOTER+MUSE sample is 0.16 ± 0.02 dex. The scatter in $[N/H]$ is $\sigma = 0.02$ dex for the XSHOOTER sample and $\sigma = 0.02$ dex for the XSHOOTER+MUSE sample. The $[N/H]$ distribution is shown in Figure 7.

The alpha element abundance $[alpha/H]$ is determined using the $^{24}Mg/^{28}Si$ ratio in the CO lines. The mean $[alpha/H]$ for the XSHOOTER sample is 0.05 ± 0.01 dex, and for the XSHOOTER+MUSE sample is 0.05 ± 0.01 dex. The scatter in $[alpha/H]$ is $\sigma = 0.01$ dex for the XSHOOTER sample and $\sigma = 0.01$ dex for the XSHOOTER+MUSE sample. The $[alpha/H]$ distribution is shown in Figure 8.

The $^{12}C/^{13}C$ ratio is determined using the $^{12}C/^{13}C$ ratio in the CO lines. The mean $^{12}C/^{13}C$ ratio for the XSHOOTER sample is 10.11 ± 0.01 , and for the XSHOOTER+MUSE sample is 10.05 ± 0.01 . The scatter in $^{12}C/^{13}C$ is $\sigma = 0.01$ for the XSHOOTER sample and $\sigma = 0.01$ for the XSHOOTER+MUSE sample. The $^{12}C/^{13}C$ distribution is shown in Figure 9.

The ^{12}CO and ^{13}CO lines are used to determine the carbon abundance. The mean ^{12}CO and ^{13}CO line ratios for the XSHOOTER sample are 0.11 ± 0.01 and 0.05 ± 0.01 , respectively, and for the XSHOOTER+MUSE sample are 0.11 ± 0.01 and 0.05 ± 0.01 , respectively. The scatter in ^{12}CO and ^{13}CO line ratios is $\sigma = 0.01$ for the XSHOOTER sample and $\sigma = 0.01$ for the XSHOOTER+MUSE sample. The ^{12}CO and ^{13}CO line ratio distribution is shown in Figure 10.

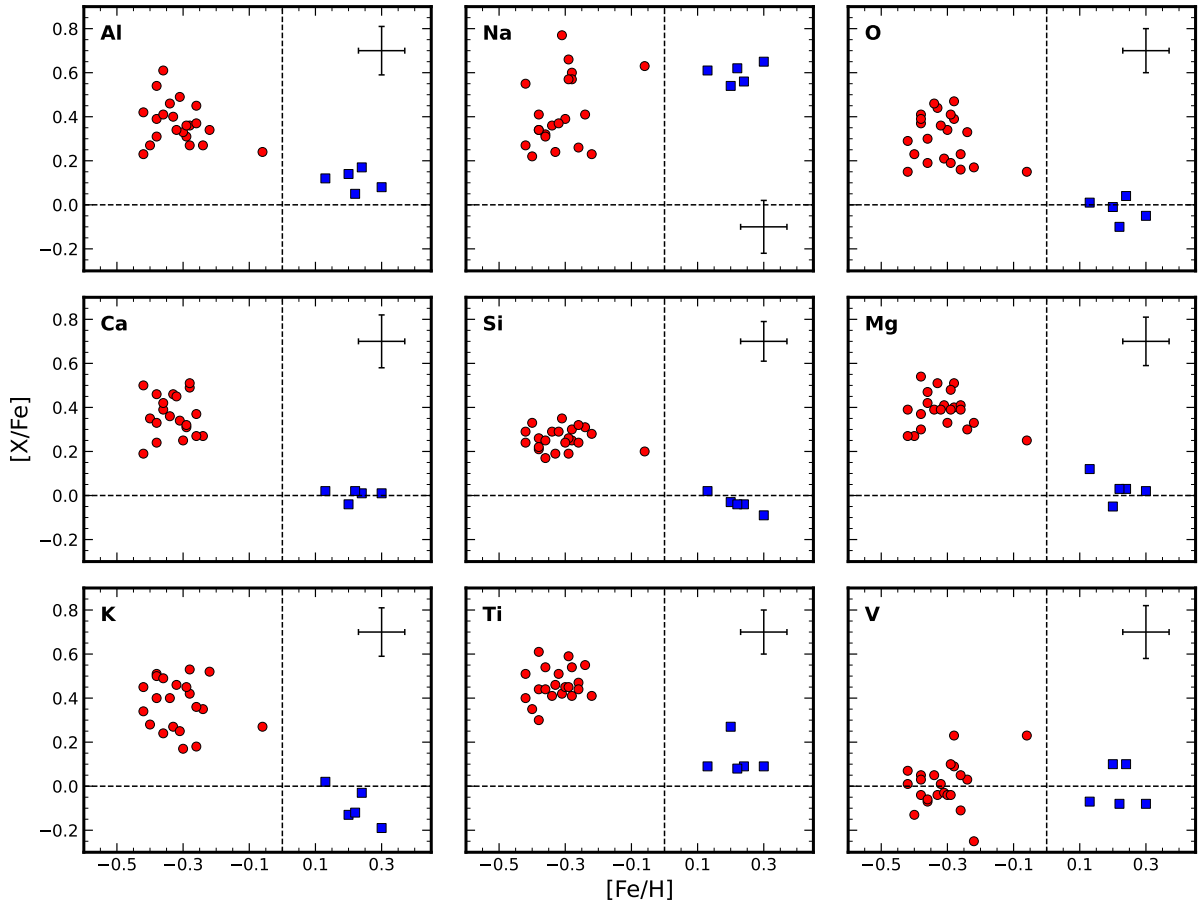


Fig. 5. $[Al/Fe]$, $[Na/Fe]$, $[O/Fe]$, $[Ca/Fe]$, $[Si/Fe]$, $[Mg/Fe]$, $[K/Fe]$, $[Ti/Fe]$, $[V/Fe]$ versus $[Fe/H]$ for the red (left) and blue (right) populations. The dashed lines indicate $[Fe/H] = 0$ and $[X/Fe] = 0$.

6. Discussion and conclusions

Our study is the first to provide a detailed chemical analysis of the GCs in the Galactic Center (GC), focusing on the α -elements and the light elements. We have identified two distinct populations: a red population and a blue population. The red population is characterized by higher α -element abundances, particularly in Al, Na, O, Ca, Si, Mg, K, Ti, and V, compared to the blue population. This is evident from the scatter plots in Figure 5, where the red circles generally show higher $[X/Fe]$ values than the blue squares for most elements. The blue population shows a pattern of lower α -element abundances, which is consistent with the characteristics of a younger, more metal-rich population. The presence of these two populations suggests a complex star formation history in the GC, involving multiple generations of stars. The red population may represent an older, more metal-poor population, while the blue population may represent a younger, more metal-rich population. This is supported by the observed differences in α -element abundances and the presence of the blue population in the GC, which is not typically seen in other Galactic populations. The study of these populations is crucial for understanding the star formation history and the chemical evolution of the GC.

The blue population is characterized by lower α -element abundances, particularly in Al, Na, O, Ca, Si, Mg, K, Ti, and V, compared to the red population. This is evident from the scatter plots in Figure 5, where the blue squares generally show lower $[X/Fe]$ values than the red circles for most elements. The presence of these two populations suggests a complex star formation history in the GC, involving multiple generations of stars. The blue population may represent a younger, more metal-rich population, while the red population may represent an older, more metal-poor population. This is supported by the observed differences in α -element abundances and the presence of the blue population in the GC, which is not typically seen in other Galactic populations. The study of these populations is crucial for understanding the star formation history and the chemical evolution of the GC.

P.B. 2012, *ICoPhA*
 Cd, 1205.004
 R.R. M., O.L., & E. 2012, *AJ*, 746, 59
 R.D., F.F.R., O.L., & 2023, *AJ*, 951, 85
 R.T. & P. 2015, *BAS*, 24, 453
 S.D.E., F.F.R., & 2015, *AJ*, 806, 152
 D.J., M.A.C., & R.P., & 2022, *MNRAS*, 513, 3429
 E., F.F.R., & O.L. 2010, *MNRAS*, 402, 1729
 E. & B.H. 2021, *MNRAS*, 505, 5978

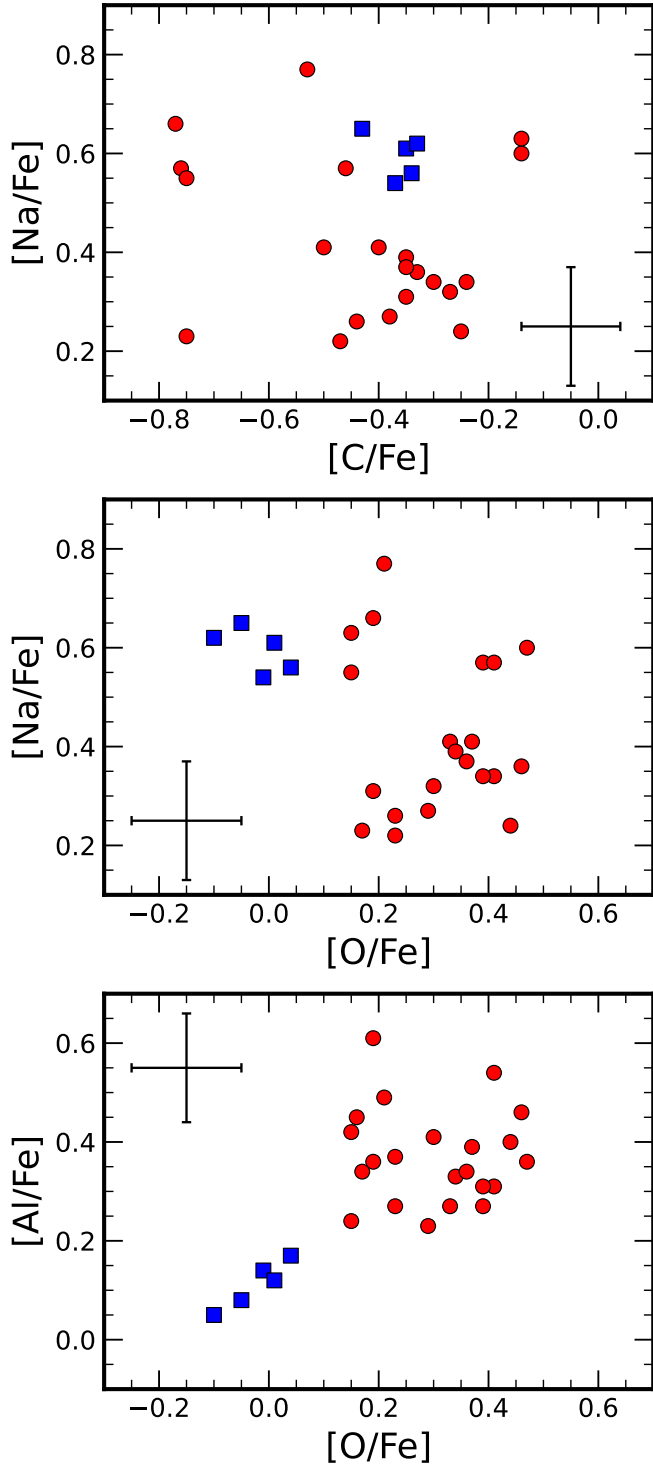


Fig. 7. $[Na/Fe]$ vs $[C/Fe]$, $[Na/Fe]$ vs $[O/Fe]$, and $[Al/Fe]$ vs $[O/Fe]$ abundance diagrams. Red circles represent the main sample, and blue squares represent the comparison sample. The crosshair indicates the position of the star HD 10180.